Size Effect on Properties of Varistors Made From Zinc Oxide Nanoparticles Through Low Temperature Spark Plasma Sintering

By *Léna Saint Macary, Myrtil L. Kahn,* Claude Estournès, Pierre Fau, David Trémouilles, Marise Bafleur, Philippe Renaud,* and *Bruno Chaudret**

Conditions for the elaboration of nanostructured varistors by spark plasma sintering (SPS) are investigated, using 8-nm zinc oxide nanoparticles synthesized following an organometallic approach. A binary system constituted of zinc oxide and bismuth oxide nanoparticles is used for this purpose. It is synthesized at room temperature in an organic solution through the hydrolysis of dicyclohexylzinc and bismuth acetate precursors. Sintering of this material is performed by SPS at various temperatures and dwell times. The determination of the microstructure and the chemical composition of the as-prepared ceramics are based on scanning electron microscopy and X-ray diffraction analysis. The nonlinear electrical characteristics are evidenced by current–voltage measurements. The breakdown voltage of these nanostructured varistors strongly depends on grain sizes. The results show that nanostructured varistors are obtained by SPS at sintering temperatures ranging from 550 to 600 °C.

1. Introduction

Zinc oxide is characterized by remarkable optical, thermal, electronic, and chemical properties. It is a wide bandgap (3.37 eV at room temperature) II–VI n-type semiconductor suitable for many applications, from solar cell electrodes,[1] which take advantage of both its optical transparency in the visible range and conductivity in thin film form, to the exploitation of high electromechanical coupling constant values as piezoelectric transducers.[2] ZnO remains the subject of much research. A central issue surrounds doping this material, in particular because p-doping is a prerequisite for its use in optoelectronics.[3] Among these present and future applications, ZnO ceramics associated with other additive oxides are well known to work as varistors, that is, these are devices which exhibit nonlinear current–voltage (*I–V*) characteristics.[4,5] Such micrometric ZnO-based varistors are widely employed and commercialized to protect electrical equipments operating at various voltage levels from degradations caused by overvoltage peaks and electrostatic discharges such as those related to lightning events in aeronautical applications.

From a practical point of view, it is usually accepted that the protection voltage is proportional to the number of grain boundaries.[6] The expansion of nanoscience over the last decades stimulated chemists so that a wide variety of nano-objects were developed and are now available by the so-called bottom-up approach.[7] Such structures have attracted much interest in the varistor world for the design of high-quality devices, since size and microstructure control are key parameters for the elaboration of nonlinear ceramics.[8] They proved useful to improve electrical characteristics; in particular, the breakdown field. However, such polycrystalline materials usually undergo a growth of their grain size during sintering[9] and the initial nanoscale is lost in the final ceramics, so that no varistor ceramics with grain-size mean diameter below 100 nm (nanostructured varistors) have been reported. The finest grained varistor ceramics described in the literature contain grains in the range of 250–500 nm in diameter.[10,11] The aim of the present study is therefore to explore a new process allowing the realization of nanostructured varistors.

Here, the use of ZnO nanoparticles synthesized by an organometallic method for the design of nanostructured varistors is reported. This method allows a good control over the size and surface state of the particles. In the present work, the most widespread varistor-forming oxide, namely bismuth oxide (Bi_2O_3), is the only added constituent for the manufacture of ceramic parts. They are thus expected to exhibit only low nonlinearity coefficients. Interestingly, the nanometric scale of

[*] Dr. M. Kahn, Dr. B. Chaudret, L. S. Macary, Dr. P. Fau
Laboratoire de Chimie de Coordination, UPR8241 CNRS
205 Route de Narbonne, 31077 Toulouse (France)
E-mail: kahn@lcc-toulouse.fr; chaudret@lcc-toulouse.fr
Dr. C. Estournès
Centre Interuniversitaire de Recherche et d'Ingénierie des Matériaux & Plateforme Nationale de Frittage Flash
Module de Haute Technologie, Université Paul Sabatier
118 Route de Narbonne, 31062 Toulouse (France)
L. S. Macary, Dr. P. Renaud
Freescale Semiconductor
134 Avenue du Général Eisenhower, 31023 Toulouse (France)
Dr. D. Trémouilles, Dr. M. Bafleur
LAAS-CNRS, Université de Toulouse
7 Avenue du Colonel Roche, 31077 Toulouse (France)

the grains was preserved by the use of a nonconventional sintering technique: spark plasma sintering (SPS).

2. Results

2.1. Synthesis

In order to test the effect of bismuth oxide addition on zinc-oxide-based ceramics, we first synthesized nanometer-scale zinc oxide powder as a reference sample. This was achieved by decomposition of an organometallic precursor in solution, namely the dicyclohexyl zinc compound [$ZnCy_2$] in tetrahydrofuran (THF). The precursor was hydrolyzed by controlled introduction of water in the solution kept under argon. If only one equivalent of water is added to the reaction medium, a yellow air-sensitive precipitate forms, which turns white when placed in contact with air or upon addition of another equivalent of water. Two equivalents of water are necessary to complete the direct formation of the final white ZnO product in solution. Once the solvent was removed by evaporation under vacuum, the white solid (Sample 1) was characterized by transmission electron microscopy (TEM) as agglomerated nanoparticles (see Fig. 1a) of approximate diameter 10 nm.

Bismuth oxide is known as one of the so-called varistor-forming oxides when associated to zinc oxide in ceramics. Varistor properties arise from the segregation of bismuth atoms at the interfaces between zinc oxide grains.[12] Consequently, we focused on obtaining a homogeneous distribution of bismuth at the nanometer scale in the synthesized powders. Thus, we performed the co-decomposition of the same organozinc precursor and a bismuth salt, namely bismuth acetate, in a one-step controlled hydrolysis. The intermediate yellow product discussed above also forms. The obtained particles (Sample 2) were similar in size and shape with Sample 1 ones, but these two samples differed in terms of agglomeration. Sample 2 was composed of well-defined isotropic nanoparticles (see Fig. 1b).

X-Ray diffraction (XRD) characterization of the as-obtained powders identifies, both for Samples 1 and 2, a wurtzite zinc oxide phase (see Fig. 2a and 2b, respectively). The extent of the crystalline domains is larger in Sample 1 than in Sample 2. The Sample 2 diffractogram shows an additional peak situated around 30°, corresponding to bismuth. However, no clues are given concerning the phase under which bismuth is found, since the peak is too broad to be analyzed. In order to gain access to more information concerning this phase, hydrolysis of bismuth acetate alone in THF was performed and the resulting white powder analyzed by XRD. The diffractogram indicated the presence of bismuth oxoacetate and unreacted bismuth acetate. It is however difficult to conclude on the presence or not of bismuth acetate in this case. Indeed, the most intense peak of bismuth oxide in its beta phase is also situated at similar angle values. High-resolution TEM (HRTEM) was performed on Sample 2 but the bismuth based phase was not located. Once dried, the nanoparticles of Sample 2 were submitted to post-synthesis annealing treatment at 400 °C for 4 h (Fig. 2c). All the diffractograms display characteristic peaks of the hexagonal ZnO phase (space group $P6_3mc$) in the 30–80° 2θ range. These peaks narrowed, indicating crystallite growth. Additional peaks appeared and were clearly identified as bismuth oxide in the beta allotropic form (Fig. 2c). The width of the corresponding peaks suggests that the β-Bi_2O_3 crystallites are larger than zinc oxide ones.

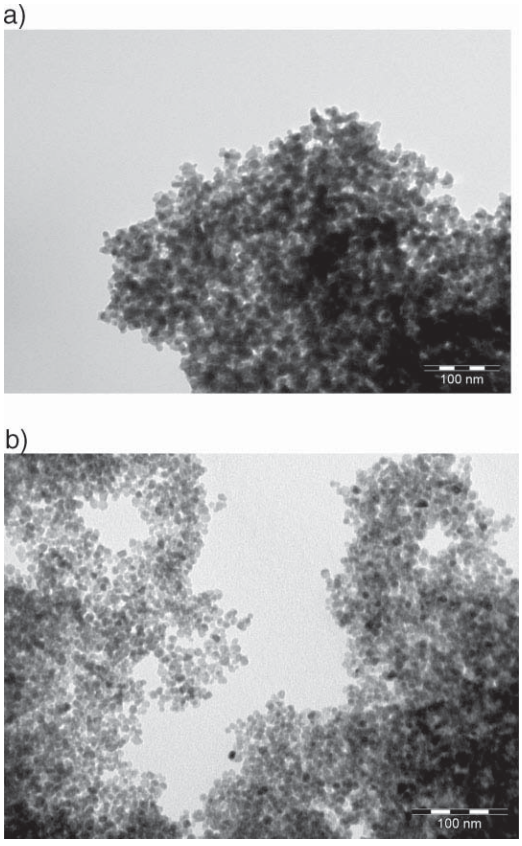

Figure 1. TEM images of nanoparticles syntheses of: a) Sample 1; b) Sample 2.

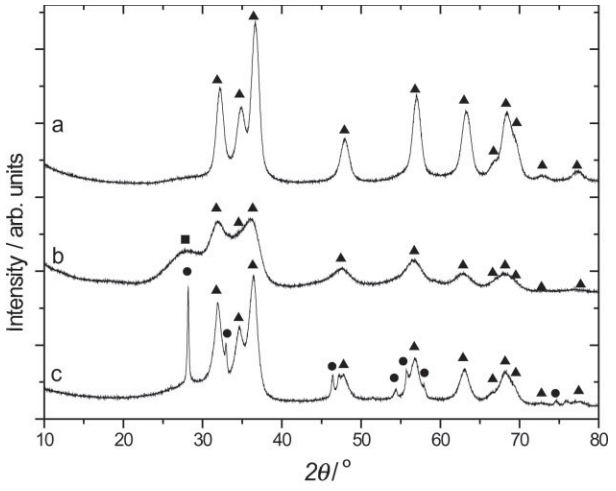

Figure 2. X-Ray diffractograms: a) Sample 1 as prepared; b) Sample 2 as prepared; and c) Sample 2 after annealing at 400 °C (▲ ZnO, ● β-Bi_2O_3, ■ not defined).

2.2. Sintering

The next step consisted of making dense nanoceramics from these nanostructured powders in order to study their electrical characteristics. Attempts to sinter pure ZnO nanopowders (Sample 1) were first carried out by the classical method. The as-prepared pellets were highly porous; their densities hardly reached 30% of pure zinc oxide (Fig. 4a). A second technique, namely SPS, was considered. It consists of hot pressing at very high heating rates. Various final temperatures and holding times were tested both for the reference powder (Sample 1) and bismuth-containing powder (Sample 2). The experimental conditions are summarized in Table 1.

During SPS, thermal shrinkage was monitored by a dilatometer, allowing insight into the sintering process. Sintering profiles differed considerably depending on the powder composition, as illustrated in Figure 3. For example, Sample 1 densification occurred between 700 and 750 °C (Fig. 3a), whereas bismuth-containing powder (Sample 2) underwent significant shrinkage at lower temperatures (between 400 and 650 °C; Fig. 3b). The important displacement observed at low temperature for Pellet 2 compared to Pellet 1 is mainly due to the fact that initial compaction prior to SPS was carried out manually. The fact that Sample 1 was not annealed prior to sintering may also partly explain this difference, as the amount of adsorbed species may be higher in this case.

Final densities of the pellets were measured using the water-immersion method. Pellets made from Sample 1 were more dense as the applied temperature was high. A densification of 90% of the theoretical density of zinc oxide (5.7 g cm^{-3}) was reached at the maximum temperature of 900 °C applied for this study. For Sample 2, it can be noted that the theoretical density (6.4 g cm^{-3}) is higher than that of pure zinc oxide due to the amount of bismuth oxide. The trend concerning the variation of density with temperatures for this composition (Sample 2) is different from that followed by pure zinc oxide materials (Sample 1), for which density increases with an increase in sintering temperature. Indeed, for Sample 2, pellets made at 800 °C are denser than the ones sintered at 900 °C (Table 1). Moreover, a step of final temperature for several minutes was found to have a considerable impact on sintering, yielding very high densities at temperatures as low as 600 °C.

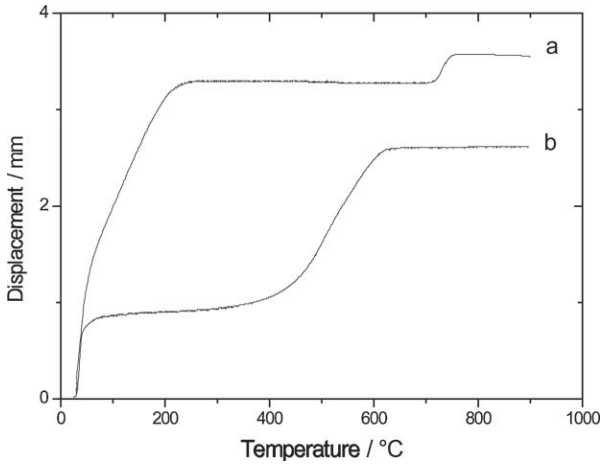

Figure 3. Sintering profiles of: a) Pellet 2 made from Sample 1; b) Pellet 11 made from Sample 2.

The pellets' microstructure was observed by scanning electron microscopy (SEM). Figure 4a–g shows characteristic SEM images of ceramics sintered from Samples 1 and 2 at various temperatures. Pellets prepared from Sample 1 by SPS at 800 °C differ considerably from those sintered in a standard furnace at 1000 °C in terms of density (4.7 and 1.7 g cm^{-3} respectively); their grain sizes, however, are similar—around a few hundred nanometers, as shown in Figure 4a and b.

Grain size increase with temperature is observed for each powder composition. For example, Pellet 1 grains, corresponding to the sintering of Sample 1 at 600 °C (Fig. 4b), are in the range of a few tens of nanometers, whereas Pellets 2 and 3, which were also made from Sample 1, exhibit grains of about 100 nm and 1 μm, respectively, as a result of SPS treatment at 800 °C for Pellet 2 and 900 °C for Pellet 3. The same trend is observed for bismuth-containing samples. In the case of Sample 2, SPS sintering at 600 °C (Pellet 6) and at 800 °C (Pellet 10) yielded grains of about 50 nm (Fig. 4f) and 1 μm (Fig. 4g), respectively. Grain size and density were also considerably modified with dwell time, as illustrated at 600 °C by the difference between Pellets 6 and 7 maintained at the final temperature for 4 and 15 min, respectively. A grain-size increase of an order of magnitude occurs and is

Table 1. Data of the pellets prepared by SPS.

Pellet	Sample	Sample annealing	Sintering T_{max} [°C] /step time [min]	Density [g cm^{-3}]	Density [%]	SEM grain size [nm]	XRD crystallite size [nm]
1	1	–	600/0	3.8	67	~10	
2	1	–	800/0	4.7	82	~100	
3	1	–	900/0	5.2	91	~2000–5000	
4	2	400 °C	500/15	4.1	65	~15	22
5	2	400 °C	550/15	5.2	83	~30–50	31
6	2	400 °C	600/4	4.6	73	~25	35
7	2	400 °C	600/15	6.1	97	~300–500	75
8	2	400 °C	650/15	5.9	94	~1000	72
9	2	400 °C	800/0	5.7	91	~1000	98
10	2	400 °C	800/0	5.8	92	~1000	83
11	2	400 °C	900/0	5.6	89	~3000–5000	>100

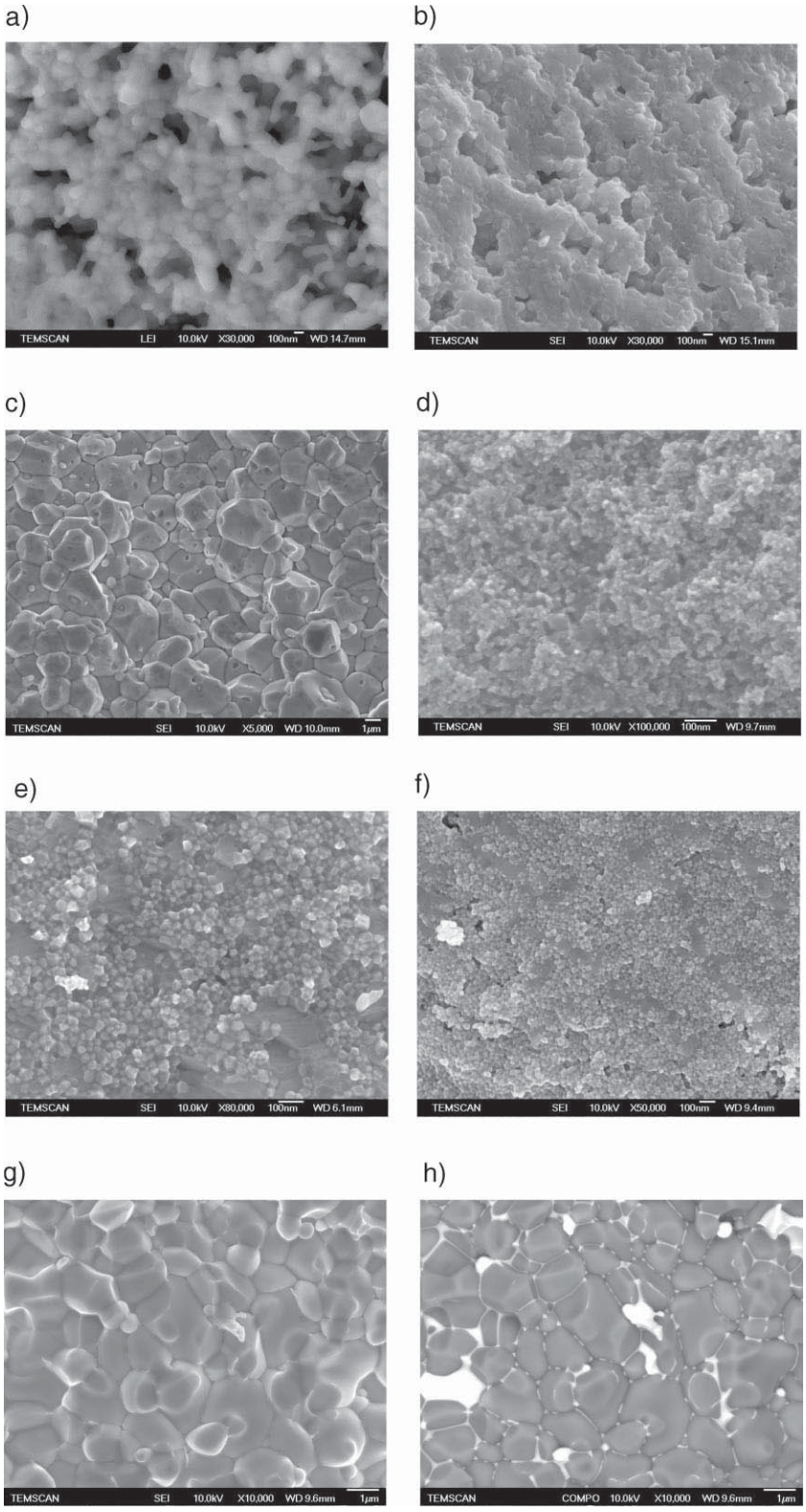

Figure 4. SEM SEI micrographs of fracture surface of: a) Sample 1 sintered at 1000 °C in a furnace; b) Pellet 2, Sample 1 sintered by SPS at 800 °C; c) Pellet 3, Sample 1 sintered by SPS at 900 °C; d) Pellet 1, Sample 1 sintered by SPS at 600 °C; e) Pellet 5, Sample 2 sintered by SPS at 550 °C for 15 min; f) Pellet 6, Sample 2 sintered by SPS at 600 °C for 4 min; g) Pellet 10, Sample 2 sintered by SPS at 800 °C; h) SEM BEI micrograph of the same image as (g).

associated with an increase in density in Pellet 7 resulting from a decrease in porosity (see Table 2). In micrometric ceramics, bismuth-rich phases are generally found to be located at multiple grain boundaries.[13,14] Backscattered electron imaging (BEI) micrographs (Fig. 4g) provide a view of the repartition of the elements in the pellets by chemical contrast imaging. Bismuth-rich phases appear in white and zinc oxide in gray, which is confirmed by X-ray microanalysis. This method shows that, in pellets sintered by SPS at high temperature, thus undergoing grain growth up to the micrometric size, bismuth is mainly found to stand at the multiple grain junctions (Fig. 4h). Some grain junctions exhibit larger amounts of bismuth, but the distribution of bismuth inside the material appears homogeneous. For Pellets 5 and 6, BEI cannot be performed at these magnifications; however, two phases can be distinguished. It can be assumed that polyhedral well-faceted grains correspond to zinc oxide, the second interpenetrated phase being identified as bismuth rich phase.

Figure 5 shows the XRD diagrams of pellets sintered by SPS at various temperatures. All diffractograms display the characteristic pattern of zincite phase in the 30–60° 2θ range. Additional peaks result from the presence of bismuth-containing phases or surface carbon contaminants (at 26.5 and 54.5°); this contamination comes from the SPS die and is further eliminated by polishing. When Pellet 4 is formed by sintering at 500 °C for 15 min, a phase transformation of bismuth oxide occurs from beta in the pristine annealed powder to α phase in the pellet (Fig. 5a). At higher temperatures, namely 600 °C, bismuth oxide further transforms into γ-Bi_2O_3 or $Bi_{38}ZnO_{58}$ ($19Bi_2O_3$:ZnO) and two other new species which are identified as metallic bismuth: one is rhombohedral (R-3m) and the other is cubic (Pm-3m). The phases γ-Bi_2O_3 and $Bi_{38}ZnO_{58}$ have identical crystal structures and can be only distinguished by a slight shift in the XRD patterns.[15] Consequently, the small intensity and large width of the corresponding peaks do not allow for discrimination between these two bismuth oxide phases. At the intermediate temperature of 550 °C, a mixture of α-Bi_2O_3, γ-Bi_2O_3, or $Bi_{38}ZnO_{58}$ and cubic bismuth is found (not shown). As for pellets sintered at 800 °C and above, bismuth is exclusively present in the rhombohedral metallic phase. The diffraction peak half-height widths of zinc oxide narrow with sintering temperature as a consequence of crystallite growth. The crystallite size was estimated using the

Table 2. Nonlinear coefficient (α) and breakdown field (V_b) or resistivity of the bismuth containing ZnO ceramics, annealed after SPS.

Pellet	T_{max} [°C]/step time [min]	Grain size [nm]	Crystallite size [nm]	α	V_b [V cm^{-1}]	ρ [kΩ cm^{-1}]
4	500/15	~15	22	N.A. [a]	N.A.	550
5	550/15	~50	31	N.M. [b]	>19000	N.A.
7	600/15	~300–500	75	5.8	10 660	N.A.
8	650/15	~1000	72	5.6	10 955	N.A.
9	800/0	~1000	98	3.6	1565	N.A.
11	900/0	~3000–5000	>100	N.A.	N.A.	2

[a] N.A: nonapplicable. [b] N.M: nonmeasureable.

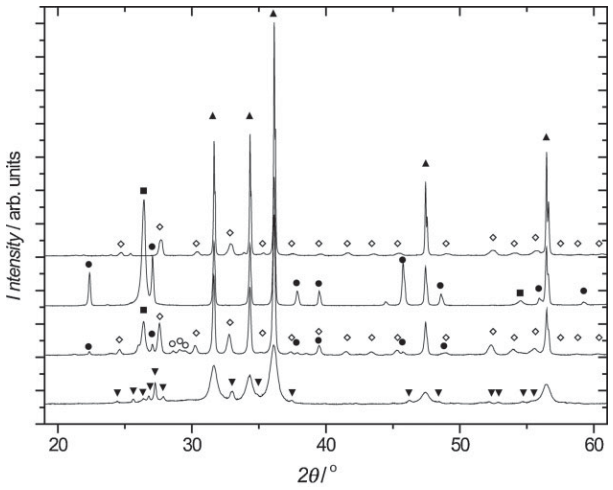

Figure 5. XRD diffractograms for: a) Pellet 4 sintered at 500 °C; b) Pellet 7 sintered by SPS at 600 °C; c) Pellet 9 as sintered at 800 °C; and d) Pellet 9 after annealing at 650 °C (▲ ZnO, ■ C, ▼ α-Bi_2O_3, ◇ γ-Bi_2O_3 or $Bi_{38}ZnO_{58}$, ● Bi, ○ Bi).

Debye–Scherrer equation up to 100 nm, since above this value the equation is not valid due to the internal line width of the diffractometer. These calculations are in good agreement with SEM grain-size observations for finely grained pellets such as Pellets 4, 5, and 6. For instance, Pellet 5 was found to contain 30-nm large crystallites, which is the grain size seen on SEM images (Fig. 4e). For pellets made at higher temperatures, the crystallite size calculated and grain size observed do not match; the grain size is larger than the calculated value. This suggests that the micrometer-sized grains observed by SEM are polycrystalline. In order to obtain a varistor, we annealed the pellets under air so as to turn the metallic bismuth phase into an oxide phase. This treatment was performed at 650 °C for 10 h and the temperature was raised at 1 °C min^{-1}. After annealing of these pellets under air at 650 °C for 10 h (see Fig. 4d), metallic bismuth turned into γ-Bi_2O_3 or $Bi_{38}ZnO_{58}$. The main bismuth-rich phase usually found in varistor ceramics made by classical sintering is the β-Bi_2O_3 phase,[10,16] but the presence of δ, γ, and α phases are also reported in some studies, depending on the additives and thermal processing conditions.[17–20] At a temperature of 650 °C, bismuth oxide and zinc oxide do not form the eutectic so that no additional sintering and no grain growth occur.

To sum up the results, ceramics are formed by SPS from binary bismuth oxide and zinc oxide nanostructured powders. After annealing of these powders, sintering is performed by SPS at low temperature as shrinkage occurs between 400 and 650 °C. By this method, ceramics with nanometer-sized grains are obtained between 500 and 600 °C. The bismuth oxide undergoes phase transformation into metallic bismuth simultaneously with densification of the pellets. The metallic bismuth phase is turned into the oxide phase again by post-sintering annealing.

2.3. Electrical Characteristics

Polycrystalline ceramics (Pellets 1, 2, and 3) prepared from pure ZnO powder (Sample 1), exhibit linear I/V characteristics with resistivities of about 20 Ω cm^{-1}. This value is slightly higher than that of pure monocrystalline zinc oxide, which generally ranges from 1 to 10 Ω cm^{-1}.[21] Pellets prepared from bismuth-containing powders (Sample 2) do not always show nonlinear behavior. Indeed, a resistive behavior is observed for pellets that have not subsequently been annealed under air after sintering. For instance, Pellets 9 and 10 prepared under the same conditions have very different electrical behavior as Pellet 10 was not annealed after sintering.

For pellets exhibiting nonlinear characteristics, following a widespread convention we determine the breakdown field as the field at which a current density of 1 mA cm^{-2} is measured. The nonlinearity coefficient α is defined as the slope of the $\log J = f(\log E)$ curve between 1 and 10 mA cm^{-2}. When the upper value of current density could not be reached, α was taken as the slope between 1 mA cm^{-2} and the last recorded point.

The results of the annealed pellets are reported in Table 2. Some annealed pellets show linear electrical behavior, namely Pellets 4 and 11. Their resistivities are also given in Table 2.

Depending on the SPS parameters, pellets annealed after sintering show different electrical behavior. Pellets 4 and 11, sintered at 500 and 900 °C, respectively, exhibit a linear behavior whereas all ceramics sintered at intermediate temperatures display a nonlinear varistor behavior (Fig. 6). For pellets exhibiting a nonlinear behavior, overall α values are low as a consequence of the simple binary composition and range from 3.6 to 5.8. The characteristic breakdown field depends on grain size observed by SEM, as generally reported. However, there is a discrepancy between Pellet 8, which has micrometric grain size and a V_b exceeding 10 000 V cm^{-1}, and Pellet 9, which has similar grain sizes but shows a ten times lower breakdown field. This

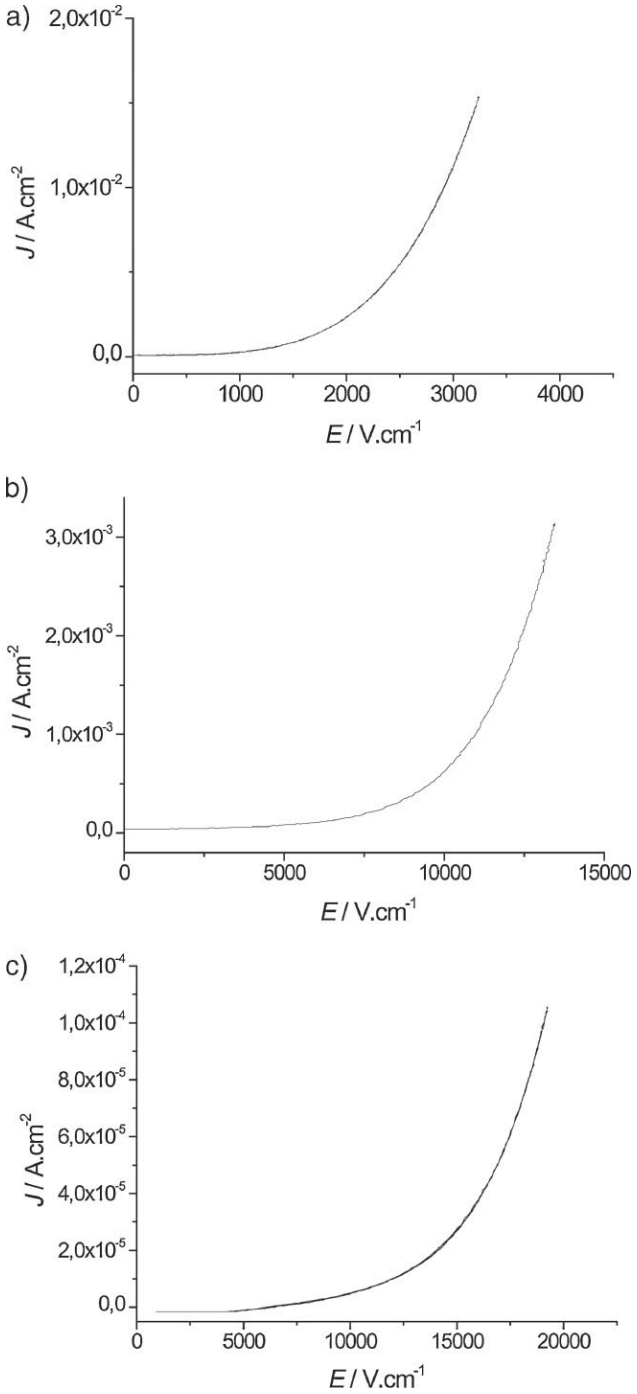

Figure 6. *I/V* curves of: a) Pellet 9; b) Pellet 8; and c) Pellet 5.

point will be further discussed. Measurement setup limitation did not allow us to extract full electrical characteristics of Pellet 5. For this pellet, the current density barely reaches 0.1 mA cm^{-2} at the maximum measurable electric field of 19 000 V cm^{-1}. Therefore, neither the breakdown field nor the nonlinearity coefficient could not be determined using the conventional criteria. A nonlinear behavior is, however, observed and, though the current density attained is not sufficient, it can be asserted that breakdown field is far above 19 000 V cm^{-1}.

3. Discussion

3.1. Synthesis

The synthesis of nanoparticles reported here is an adaptation of the method we previously described.[22,23] This reaction involves the hydrolysis of the organometallic precursor [$ZnCy_2$] in solution. The main improvement consisted of performing a controlled hydrolysis reaction by adding dropwise an organic solution containing two equivalents of water under inert atmosphere so as to grant the reproducibility of hydrolysis conditions. Moreover, to meet the goals of this work, namely the preparation of nanostructured varistors from wet organometallic chemistry, the synthesis was developed so as to fulfill the requirements of the SPS technique. First of all, in order to provide sufficient amounts of material (grams) for sintering while using reasonable quantities of solvent for the synthesis, the concentration of the reacting solution was multiplied by more than 10. Finally, we abandoned the use of stabilizing agents such as amine ligands, because they cause the powders to leak out of the SPS die at low temperature. When [$ZnCy_2$] alone was hydrolyzed without surfactants (Sample 1), the only possible stabilizing agent was the solvent itself, which turns out to be efficient enough to yield nanoparticles but not to keep them in the colloidal state as they agglomerate and precipitate. The case of Sample 2, which involves the co-hydrolysis of dicyclohexylzinc and bismuth acetate, is, however, somehow different because of the presence of acetate in the reaction solution. The hydrolysis of the bismuth salt releases acetic acid that may account for the less agglomerated state of the nanoparticles. Indeed, carboxylic acids are likely to stabilize nanoparticles synthesized by this organometallic method, since long chain alkyl carboxylic acids are widely employed.[24,25]

We chose to start our study with the most studied oxides used in the formulation of varistors, namely zinc and bismuth oxides. Regardless of nonlinearity coefficient, we essentially focused on making nanostructured varistors and studying the influence of the enhanced number of grain boundaries per thickness unit on breakdown field. Usually, the amount of bismuth oxide used for varistor ranges from 0.5 to 1 mol%.[14,16,26] The surface to volume ratio is considerably higher in the case of nanoparticles when compared to micrometric powders. Therefore, we adapted the bismuth precursor quantity accordingly and focused our study on 0.08 M equivalents of bismuth precursor for the synthesis of the particles which corresponds to 3.7 mol % Bi_2O_3.

3.2. Nanoparticles for Varistor Elaboration and SPS for Nanostructured Ceramics Formation

Several papers report on the use of nanoparticles as building blocks for the formation of high-voltage breakdown varistors but the description of nanostructured varistors by classical sintering is lacking. In general, particles ranging from 20 to 50 nm are reported as raw materials. These latter, however, undergo grain growth during sintering to attain 250 nm to ~10 μm in the final varistor material.[27,28] Only one paper reports the preparation of a varistor starting from zinc oxide nanoparticles as small as 8 nm.[8]

However, in this paper, varistors are sintered by the classical method, and due to their high surface reactivity, the nanoparticles grow during sintering and the size of the final grains is very large, ~10 μm.

We envisioned that by combining the fine organometallic synthesis of few nanometer zinc oxide particles and the fast heating rates of the SPS technique, we might succeed in preparing nanostructured varistors. Indeed, it is well known that SPS allows the formation of well-densified ceramics without an excessive grain growth of the starting nanomaterial and limits interdiffusions in the case of materials association.[29–32] For example, nanoceramics of various metal oxide materials such as Al_2O_3,[33] MgO,[34] TiO_2,[35,36] $BaTiO_3$,[36] ZrO_2,[37] SiAlON,[38] hydroxy-apatites,[39] Y_2O_3,[40] and ZnO[41] have been successfully prepared by this method. In the case of zinc oxide, no nanostructured varistor ceramic has been described, mainly because the reported works are either focused on other applications,[41] or the final material is not nanometer-scaled.[42] However, Gao et al.[43] report the formation of a nanostructured (~100 nm) ceramic by SPS exclusively made of zinc oxide that exhibits nonlinear electrical characteristics. We did not observe the same behavior with pure zinc oxide grains: in our case, bismuth oxide introduction was found to be necessary in order to obtain the nonlinearity behavior. In the present work, varying SPS temperature and dwell time parameters, we find that in order to keep nanometer-sized grains (i.e., <100 nm) in the presence of bismuth oxide a temperature window between 500 and 600 °C is suited. Moreover, density measurements show that among these ceramics, those sintered with a temperature step of 15 min were better densified. For example, Pellet 6 sintered at 600 °C for 4 min is 73% dense whereas Pellet 7, sintered for 15 min is 97% dense. A moderate grain growth is associated to this increase in density. Indeed, a final grain size of a few hundred nanometers is observed for Pellet 7. Our goal being to keep a nanometer grain size as well as to reach the highest possible density of the ceramic, a good balance is found for Pellet 5, which was sintered at 550 °C for 15 min. In this case, the grain size ranges between 30 and 50 nm and 83% density is reached. This latter value of density is not very high for varistor ceramics, however, Pellet 5 showed interesting electrical characteristics (see below).

3.3. Influence of Phase Transformation on the Sintering Process SPS

The systematic study of the XRD diagram of the pellets sintered at various temperatures allows establishing that a partial to complete reduction of bismuth oxide into metallic bismuth occurs above 550 °C. This unexpected result originates from the particular experimental conditions in which the SPS is performed, i.e., the oxide nanoparticles are in a graphitic die that, combined with the low oxygen partial pressure in the chamber under vacuum, can promote the reduction of bismuth oxide. Sintering or annealing a varistor in a reducing atmosphere is known to damage its properties as a result of the collapse of potential barriers at grain boundaries.[44,45] We also observed such an effect, which may even be enhanced in our case by the formation of metallic bismuth creating short circuits; for instance, Pellet 10 has a linear electrical characteristic (250 Ω cm^{-1}). We overcome this difficulty by annealing the pellets under air after SPS (650 °C, 10 h) so that, for example, Pellet 9, sintered in the same conditions as Pellet 10 but subsequently annealed, shows a nonlinear behavior. Interestingly, this reduction of bismuth oxide into metallic bismuth brings an unexpected sintering aid as it drastically contributes to the densification. For example, over 25% of density is gained between Pellet 4 sintered at 500 °C, a temperature at which the reduction has not begun, and Pellet 5 sintered at 550 °C, a temperature at which reduced bismuth can be found. The effect of metallic bismuth is also dramatic on the ceramic's morphology. Indeed, pellets sintered without bismuth, as Pellet 2, exhibit ten times smaller grain sizes than those sintered in the same conditions in the presence of bismuth (see Pellets 9 and 10, for example). Such results may come from a similar liquid-phase-assisted sintering mechanism that is usually observed at higher temperature when classical sintering is used.[46,47] Indeed, both XRD and BEI observations confirm the presence of the metallic bismuth phase wetting the ZnO grains (Fig. 4h). The difference between classical varistor sintering and SPS is that for SPS, the reduction of bismuth oxide into metallic bismuth is likely to form a liquid phase far below the ZnO-Bi_2O_3 binary-system eutectic (740 °C). This low temperature formation of a liquid phase accounts for: i) the important densifications obtained at such low temperatures (97% at 600 °C in Pellet 7), more than 300 °C inferior to the temperature usually reported in the case of classical sintering, and ii) the observation of nonlinearity for I–V characteristics for pellets sintered as low as 550 °C.

3.4. Influence of Grain Size and Temperature Processing on the Electrical Characteristics

The electrical characteristics of the annealed pellets exhibit a current density passing through the pellets sintered between 550 to 800 °C that does not vary linearly with the applied electric field. The α values are comparable to those commonly reported in the literature for binary composition restrained to zinc oxide and bismuth oxide (less than 8).[48,49] For Pellets 7 and 8 sintered by SPS respectively at 600 and 650 °C, the grain size was evaluated to be equal to 300–500 nm and to 1 μm, respectively. The breakdown field values (~10 000 V cm^{-1}) measured for these pellets are comparable to the ones reported in the literature for comparable grain size ceramics. Indeed, ZnO varistors containing grains of 250–500 nm, which are the smallest reported in the literature, possess breakdown field values in the range of 15 000–40 000 V cm^{-1}.[11] They were obtained by sintering at 750 °C a 2–4-μm-thick film. Similar electrical results are described by Duran et al.[10] with pellets densified by a two-step sintering process at 900 and 825 °C and whose grain size is around 500 nm. In this case, the breakdown field value is in the range of 10 000–20 000 V cm^{-1}.

As expected, we also observed that the breakdown field value greatly depends on the pellet's microstructure, and varies inversely with the average grain size of the ZnO matrix. For example, the breakdown field values increase between Pellets 7 and 5, and at the same time the grain sizes decrease by a factor of 10. In the case of Pellets 7 and 8, the link between the breakdown field value and the grain size is not obvious as they both have the

same value of breakdown field although the corresponding grain sizes differ by a factor of 2. However, it is well known that the evaluation of grain size from SEM images can only give a rough estimate, so the grain sizes in Pellets 7 and 8 may actually not greatly differ. Only Pellet 9 does not follow this trend, as it shows low breakdown field value (1 500 V cm^{-1}) compared to that of Pellet 8 (11 000 V cm^{-1}) even though both pellets contain grains of the same size. The temperature at which Pellet 9 is formed by SPS (800 °C) may be high enough to lead to the evaporation of liquid metallic bismuth similarly to bismuth oxide evaporation occurring in classical sintering.[50] Consequently, the amount of bismuth left is not sufficient to create active potential barriers at all grain boundaries, which accounts for the decrease in breakdown-field values. Bismuth evaporation also accounts for the linear behavior of Pellet 11 sintered at even higher temperature (900 °C). This hypothesis is strengthened by the decrease of the density values measured for Pellet 9 (5.7 g cm^{-3}), sintered at 800 °C, and Pellet 11 (5.6 g cm^{-3}), sintered at 900 °C, which tend towards the density of pure zinc oxide. The vacuum pressure variations with temperature also endorse the proposal that metallic bismuth evaporates at temperatures above 650 °C. Indeed, three pressure increases measured in the vacuum chamber can be distinguished: i) the first one is around 150 °C; it is linked to desorption of adsorbed species from the surface of the particles such as water, for example; ii) the second one occurs between 450 and 650 °C, that is to say in the temperature range at which shrinkage and phase transformations occur. Thus, it may be related to the release of oxygen caused by the reduction of bismuth oxide into metallic bismuth; iii) the last one is recorded between 650 and 900 °C, which we attribute to the evaporation of metallic bismuth.

No varistor ceramic constituted of grains of size as small as 50 nm was ever elaborated. Pellet 5 sintered by SPS at 550 °C is the first example at such low scale. From the nonlinearity of the curve and the 0.1 mA cm^{-2} reached at the maximum applicable field (19 000 V cm^{-1}), we can assert that the breakdown field value is among the highest ever measured. The number of grains contained in Pellet 5 is 20 times higher than the one contained in Pellet 8 for the same thickness (1 mm). In order to measure the contribution of the same average number of grains in the two above mentioned pellets, Pellet 5 would have to be thinned down to 50 μm, allowing access to an estimated maximum electric field of 300 000 V cm^{-1}.

4. Conclusions

Organometallic synthesis provided a $ZnO–Bi_2O_3$ nanomaterial (10 nm) well suited as a raw material for the formation of two-component varistors. The use of SPS to shape and densify the powders into pellets results in a reduction of bismuth oxide into metallic bismuth. This constitutes an unexpected and significant sintering aid and promotes low-temperature sintering thus allowing the preparation of nanostructured varistors. These varistors exhibit a nonlinear behavior and the dependence of the breakdown field on the material grain size is further demonstrated with a clear shift of the breakdown field to high values observed for nanostructured ceramics. Such an approach has a high potential of development since the versatility of the synthetic approach allows the addition of other oxides known to improve varistor nonlinearity (Co, Mn, etc.).[51–54] This work may open new ways for the elaboration of nanodevices.

5. Experimental Section

Synthesis: Pure Zinc Oxide Materials: Two equivalents of water were added dropwise to a 4.32 M THF solution of [$ZnCy_2$] via a wet solution of THF containing 10 300 ppm of water. After the solution turned dark yellow, a white solid precipitated within minutes. THF was evaporated to dryness under vacuum. A white powder was obtained.

Zn/Bi Mixed Metal Oxide Materials: A 0.08 M equivalent of bismuth triacetate (III) was added to a 4.32 M THF solution of [$ZnCy_2$]. The solution was kept under stirring for 10 min in order to achieve the complete dissolution of bismuth triacetate (III). Two equivalents of water were then added dropwise. The solution turned yellow then white and a precipitate formed. The powders were dried under vacuum and then annealed at 400 °C for 4 h under air.

XRD: The powder's and pellet's XRD patterns were collected on a XPert Pro (θ–θ mode) Panalytical diffractometer with $\lambda(CuK_{\alpha 1}, K_{\alpha 2}) = 1.54059$, 1.54439 Å, respectively. The extraction of peak positions for indexing was performed with the fitting program, available in the PC software package Highscore + supplied by Panalytical. The phase identification was performed with ''searchmatch'' in Highscore +, based on the PDF2 ICCD database.

TEM/SEM: The TEM specimens were prepared by slow evaporation of solution droplets of the different samples deposited on carbon-supported copper grids. The experiments were performed on a JEOL JEM-1011. The size distribution was determined manually by an analysis of low-magnification TEM images. In this procedure, the different particles were visually identified according to an upper and lower intensity threshold and then counted and measured. This analysis was made only on isolated particles which are not numerous in the case of agglomerated particles, thus giving only an estimate of the particle size.

SEM specimens were prepared as follows: the powder samples were either deposited on a silicon substrate or glued directly on the aluminum sample holder via a silver paste. Pellets were directly stuck to the aluminum sample holder by a carbon-double-face tape. SEM measurements were performed on a field emission gun scanning electron microscope JEOL 6700F. Micrographs were collected using secondary electron imaging (SEI) for the topographical mode and in compositional mode by back-scattered electron imaging (BEI). X-Ray analysis was performed using the SEM interfaced with a Princeton Gamma-Tech energy dispersive X-ray (EDX) microanalysis system.

Sintering: Classical Sintering: Pellets were prepared by uniaxial pressing (1500 MPa) ZnO powders in a 5-mm-diameter die. Usual sintering process under air was performed in a compact tube furnace RS50/300/11 from Nabertherm equipped with a C40 program controller at a maximum temperature ranging from 850 to 1000°C. The heating rate from room temperature to 400 °C was 1 °C min^{-1}; above 400 °C the temperature was raised by 2 °C min^{-1} up to the maximum temperature, which was held for 2 h. The cooling rate was 1.5 °C min^{-1}.

Spark Plasma Sintering: Samples were sintered using a Dr Sinter 2080 SPS apparatus (SPS Syntex Inc., Tokyo, Japan). Precursor's powders (without any sintering aids) were loaded onto an 8-mm inner-diameter cylindrical die and placed in a chamber under vacuum. The pulse sequence was 12-2 (pulses–dead time or zero current), with each pulse lasting 3.3 ms.[55] The temperature was automatically raised from room temperature, monitored, and regulated to the final temperature (500–800 °C range) by a thermocouple introduced in a small hole located at the surface of the die. A heating rate of 50 °C min^{-1} was used to reach the final temperature. The cooling conditions were not forced: once the maximum temperature was reached, heating was stopped and the pellets were left to cool down to room temperature. Uniaxial pressure of 50 MPa was applied progressively in the first minute and held until completion of the temperature step at final temperature (held from 0 to 15 min). In these

conditions, the current passing through the die and the voltage reached maximum values of 300 A and 3 V, respectively.

Electrical Measurements: The sintered pellet surfaces were polished using various grades of SiC abrasive papers (Presi P600 and P1200) down to a thickness of about 1 mm in order to eliminate the carbon surface contamination induced by the use of graphitic dies. Gold electrodes were further deposited on both sides of the pellets by sputtering on an Alcatel 450 sputtering machine. Electrical measurements were performed on a HP4142B Modular DC Source Monitor limited to 200 V in absolute value. These measurements were completed when necessary on a 370A Programmable Curve Tracer from Sony Tektronix attaining 2000 V.

Acknowledgements

This research was carried out within the framework of LISPA joint lab between Freescale Semiconductor and the Centre National de la Recherche Scientifique, CNRS supported by the French Ministry of Industry, Midi-Pyrénées Regional Council, Haute-Garonne Council and Grand Toulouse. The authors thank TEMSCAN service for TEM measurements, Vincent Collière for SEM and HRTEM measurements, Ludovic Salvagnac for sputtering deposition and Laure Vendier for XRD measurements. Supporting Information is available online from Wiley InterScience or from the author.

[1] W. Beyer, J. Huepkes, H. Stiebig, *Thin Solid Films* **2007**, *516*, 147.
[2] Z. L. Wang, *Appl. Phys. A* **2007**, *88*, 7.
[3] D. C. Look, B. Claflin, *Phys. Status Solidi B* **2004**, *241*, 624.
[4] D. R. Clarke, *J. Am. Ceram. Soc.* **1999**, *82*, 485.
[5] T. K. Gupta, *J. Am. Ceram. Soc.* **1990**, *73*, 1817.
[6] M. Bartkowiak, G. D. Mahan, F. A. Modine, M. A. Alim, R. Lauf, A. McMillan, *J. Appl. Phys.* **1996**, *80*, 6516.
[7] Y. Liu, Y. Tong, *J. Nanosci. Nanotechnol.* **2008**, *8*, 1101.
[8] M. Singhal, V. Chhabra, P. Kang, D. O. Shah, *Mater. Res. Bull.* **1997**, *32*, 239.
[9] S. C. Pillai, J. M. Kelly, D. E. McCormack, P. O'Brien, R. Ramesh, *J. Mater. Chem.* **2003**, *13*, 2586.
[10] P. Duran, F. Capel, J. Tartaj, C. Moure, *Adv. Mater.* **2002**, *14*, 137.
[11] Y. Q. Huang, L. Meidong, Z. Yike, L. Churong, X. Donglin, L. Shaobo, *Mater. Sci. Eng, B* **2001**, *B86*, 232.
[12] F. Greuter, *Solid State Ionics* **1995**, *75*, 67.
[13] D. R. Clarke, *J. Appl. Phys.* **1978**, *49*, 2407.
[14] K.-I. Kobayashi, O. Wada, M. Kobayashi, Y. Takada, *J. Am. Ceram. Soc.* **1998**, *81*, 2071.
[15] J. P. Guha, Š. Kunej, D. Suvorov, *J. Mater. Sci.* **2004**, *39*, 911.
[16] W. Onreabroy, N. Sirikulrat, A. P. Brown, C. Hammond, S. J. Milne, *Solid State Ionics* **2006**, *177*, 411.
[17] S. Bernik, S. Macek, B. Ai, *J. Eur. Ceram. Soc.* **2001**, *21*, 1875.
[18] S. Ezhilvalavan, T. R. N. Kutty, *Mater. Chem. Phys.* **1997**, *49*, 258.
[19] E. Olsson, G. L. Dunlop, *J. Appl. Phys.* **1989**, *66*, 3666.
[20] E. Olsson, G. L. Dunlop, R. Oesterlund, *J. Appl. Phys.* **1989**, *66*, 5072.
[21] K. Ellmer, *J. Phys. D: Appl. Phys.* **2001**, *34*, 3097.
[22] M. L. Kahn, M. Monge, V. Collière, F. Senocq, A. Maisonnat, B. Chaudret, *Adv. Funct. Mater.* **2005**, *15*, 458.
[23] M. Monge, M. L. Kahn, A. Maisonnat, B. Chaudret, *Angew. Chem. Int. Ed.* **2003**, *42*, 5321.
[24] M. L. Kahn, M. Monge, E. Snoeck, A. Maisonnat, B. Chaudret, *Small* **2005**, *1*, 221.
[25] C. Pagès, Université Paul Sabatier, Toulouse **2007**.
[26] E. Olsson, G. L. Dunlop, *J. Appl. Phys.* **1989**, *66*, 4317.
[27] Y. Kang Xue, D. Wang Tian, Y. Han, D. Tao Min, J. Tu Ming, *Mater. Res. Bull.* **1997**, *32*, 1165.
[28] Y. Lin, Z. Zhang, Z. Tang, F. Yuan, J. Li, *Adv. Mater. Opt. Electron.* **2000**, *9*, 205.
[29] M. N. Zhijian Shen, *Chem. Rec.* **2005**, *5*, 173.
[30] R. Chaim, M. Levin, A. Shlayer, C. Estournes, *Adv. Appl. Ceram.* **2008**, *107*, 159.
[31] M. M. Catherine Elissalde, C. Estournès, *J. Am. Ceram. Soc.* **2007**, *90*, 973.
[32] U. C. Chung, C. Elissalde, M. Maglione, C. Estournes, M. Pate, J. P. Ganne, *Appl. Phys. Lett.* **2008**, *92*, 042902/1.
[33] R. S. Mishra, J. A. Schneider, J. F. Shackelford, A. K. Mukherjee, *Nanostruct. Mater.* **1995**, *5*, 525.
[34] R. Chaim, Z. Shen, M. Nygren, *J. Mater. Res.* **2004**, *19*, 2527.
[35] P. Angerer, L. G. Yu, K. A. Khor, G. Krumpel, *Mater. Sci. Eng, A* **2004**, *A381*, 16.
[36] M. T. Buscaglia, V. Buscaglia, M. Viviani, J. Petzelt, M. Savinov, L. Mitoseriu, A. Testino, P. Nanni, C. Harnagea, Z. Zhao, M. Nygren, *Nanotechnology* **2004**, *15*, 1113.
[37] U. Anselmi-Tamburini, J. E. Garay, Z. A. Munir, A. Tacca, F. Maglia, G. Spinolo, *J. Mater. Res.* **2004**, *19*, 3255.
[38] X. Xu, T. Nishimura, N. Hirosaki, R.-J. Xie, Y. Yamamoto, H. Tanaka, *Nanotechnology* **2005**, *16*, 1569.
[39] C. Drouet, F. Bosc, M. Banu, C. Largeot, C. Combes, G. Dechambre, C. Estournès, G. Raimbeaux, C. Rey, *Powder Technol* **2009**, *190*, 118.
[40] R. Chaim, A. Shlayer, C. Estournes, *J. Eur. Ceram. Soc.* **2009**, *29*, 91.
[41] J. Wang, L. Gao, *J. Am. Ceram. Soc.* **2005**, *88*, 1637.
[42] F. Luo, J. He, Y. Lin, J. Hu, *Key Eng. Mater.* **2008**, *368–372*, 514.
[43] L. Gao, Q. Li, W. Luan, H. Kawaoka, T. Sekino, K. Niihara, *J. Am. Ceram. Soc.* **2002**, *85*, 1016.
[44] A. Glot, E. Di Bartolomeo, A. Gaponov, R. Polini, E. Traversa, *J. Eur. Ceram. Soc.* **2004**, *24*, 1213.
[45] E. Sonder, M. M. Austin, D. L. Kinser, *J. Appl. Phys.* **1983**, *54*, 3566.
[46] J.-H. Choi, N.-M. Hwang, D.-Y. Kim, *J. Am. Ceram. Soc.* **2001**, *84*, 1398.
[47] J.-R. Lee, Y.-M. Chiang, *Solid State Ionics* **1995**, *75*, 79.
[48] W. G. Morris, *J. Am. Ceram. Soc.* **1973**, *56*, 360.
[49] J. Wong, *J. Am. Ceram. Soc.* **1974**, *57*, 357.
[50] M. A. de la Rubia, M. Peiteado, J. F. Fernandez, A. C. Caballero, *J. Eur. Ceram. Soc.* **2004**, *24*, 1209.
[51] S. Ezhilvalavan, T. R. N. Kutty, *J. Mater. Sci. Mater. Electron.* **1996**, *7*, 137.
[52] J. Han, A. M. R. Senos, P. Q. Mantas, *J. Eur. Ceram. Soc.* **2002**, *22*, 1653.
[53] Y. W. Hong, J. H. Kim, *Ceram. Int.* **2004**, *30*, 1301.
[54] W. Onreabroy, N. Sirikulrat, *Mater. Sci. Eng, B* **2006**, *130*, 108.
[55] W. Chen, U. Anselmi-Tamburini, J. E. Garay, J. R. Groza, Z. A. Munir, *Mater. Sci. Eng, A* **2005**, *394*, 132.